Nuclear Instruments and Methods in Physics Research A 821 (2016) 44–54

Contents lists available at ScienceDirect

Nuclear Instruments and Methods in Physics Research A

journal homepage: www.elsevier.com/locate/nima

Focusing neutron reflectometry: Implementation and experience on the TOF-reflectometer Amor

J. Stahn *, A. Glavic

Paul Scherrer Institut, Laboratory for Neutron Scattering and Imaging, 5232 Villigen PSI, Switzerland

ARTICLE INFO

Article history:
Received 30 November 2015
Received in revised form
4 February 2016
Accepted 2 March 2016
Available online 5 March 2016

Keywords:
Reflectometry
Neutron
Focusing

ABSTRACT

Neutron reflectometry is a powerful tool to investigate chemical and magnetic depth profiles near surfaces. The advantages of neutrons compared to x-rays are their sensitivity to isotopes, the high penetration capabilities and the high sensitivity to magnetic induction. The biggest disadvantage however is the low flux available, which leads to much longer counting times on much larger samples.

In order to boost the performance of neutron reflectometers, a focusing guide system was developed and realised over recent years. Here we report on the application and performance of a down-scaled demonstrator of such a *Selene* guide, installed as an add-on on the time-of-flight (TOF) reflectometer Amor at the PSI. Due to the limited size of the guide, the flux is concentrated to a footprint of at most 2 mm width. It is thus possible to avoid illumination of contacts even on small samples. Despite the fact that typical samples measured on Amor with a size of 10×10 mm^2 are markedly under illuminated, the presented set-up leads to a reduction in counting time of 80%. The use of the demonstrator thus allows for in-situ or in-operando investigations with a time resolution of a few minutes for a q_z range from 0.005 Å^{-1} to 0.08 Å^{-1}.

Besides a short recapitulation of the concept of focusing reflectometry, a detailed description of the data reduction and its quality is given, followed by an application example.

1. Introduction

Reflectometry is a method to probe densities of flat samples near the surface. In this paper only the depth-profile (averaged parallel to the surface) is regarded. This means we concentrate on specular reflectometry here. The quantity actually probed and what *near* means depends on the radiation used. In the present case with cold neutrons the reflectivity contains information about the depth profile of the average nuclear (isotope) density and the in-plane magnetic induction. The depth resolution reaches from the sub-nm range up to a fraction of a μm, where the limits are imposed by the measurement range and the instrumental resolution.

The principle is that a defined beam hits the surface under investigation at a grazing angle and is partly transmitted and partly reflected there. The measured quantity is the intensity of the reflected beam, to which the reflectance of the surface and of all the parallel interfaces underneath contribute. In a simplified picture the contrast between the layers defines the amplitude and the thicknesses of the films the phase of the reflected neutron. The measured signal is the result of the interference of all reflected waves. For a quantitative interpretation of the data one has to compare the measured reflectivity to one calculated on the basis of an assumed model. The calculation requires the solution of the wave equation for the neutron interacting with all interfaces simultaneously [1].

The strength of neutrons compared to the much cheaper x-rays is that they are sensitive to light elements and isotopes, have a higher penetration depth, are sensitive to magnetism, and that they can easily penetrate through the sample environment allowing for extreme temperatures, magnetic fields and pressure. This makes them an ideal probe to investigate for example biological membranes, absorbed layers at solid or liquid surfaces, diffusion between layers, magnetic depth profiles in artificial heterostructures or multiferroic films, and many more.

The drawback of neutron reflectometry is that the measurement time is quite long. Depending on the source, the sample size and the scientific question data collection periods range from a few seconds up to a day for one reflectivity curve, seconds are the exception.

In the following we present an approach of how to speed up the measurements by an order of magnitude for small samples, where small means that the sample width is below the achievable beam spot size. In the presented set-up this means a width of

* Corresponding author.
E-mail addresses: jochen.stahn@psi.ch (J. Stahn), artur.glavic@psi.ch (A. Glavic).

http://dx.doi.org/10.1016/j.nima.2016.03.007

2 mm, for a full-scale realisation up to 20 mm can be reached. A detailed description of the experimental set-up and the data reduction is given, followed by an example.

2. Concept of focusing, high-intensity reflectometry

To obtain the specular reflectivity $R(q_z)$ one has to measure the intensity of a beam reflected from a surface with the momentum transfer q_z normal to the surface. There are two conventional approaches to scan $q_z = \frac{4\pi}{\lambda} \sin\theta$. Either the wavelength λ is kept fix and the angle of incidence θ is varied (angle-dispersive set-up) or θ is kept constant and λ is varied (energy-dispersive set-up). The latter is realised by using a pulsed neutron beam, where the travelling time from the pulse generator (the source or a chopper) to the detector is measured. This time is directly proportional to λ. In both setups, the instrumental resolution is determined by the angular resolution σ_θ, given by the slit and sample geometry, and by the wavelength resolution σ_λ, determined by the monochromator or the pulse duration and flight path length.

In order to reduce the counting time for specular reflectometry measurements on continuous sources, R. Cubitt suggested to use a well-collimated white beam incident on the sample and to spectrally analyse the reflected beam by using a refractive prism. A position-sensitive detector is then used to detect the refraction angles and thus the wavelengths. In this RAINBOWS concept [2] the flux gain is proportional to the wavelength band (and the related incident intensity), reduced by the projection of the beam footprint on the sample to the detector. The latter is limited by the prism size and the angular resolution of the set-up.

An other approach is the REFOCUS concept by Ott [3]. He suggested to encode λ in θ in a beam of wide divergence focused to the sample. The impact location of the reflected neutron on the position sensitive detector then is used to obtain θ and in consequence also λ. In this concept the beam is prepared by a planar-elliptic reflector with a graded monochromating coating. This approach would increase the flux on the sample by an order of magnitude. But the resolution function $\sigma_\theta(\lambda)$ as obtained with the suggested graded monochromator is not acceptable. An alternative approach is to use a coating which reflects all wavelengths (up to a technical threshold) and to realise the encoding by reflection of the neutrons on a q_z-bandpass mirror[1] at the initial focal point of the ellipse.

We adapted the idea of using a focused beam and to measure θ with the detector to a time-of-flight instrument. Here no wavelength encoding is necessary for specular reflectometry and thus the full pulsed beam is sent to the sample. This approach sacrifices the ability to measure specular and off-specular reflectivity simultaneously, but the flux gain on the sample for specular measurements is proportional to $\Delta\theta/\sigma_\theta$. This means an increase in flux by more than an order of magnitude for small and moderate q_z, and a bit less for very high q_z.

Most neutron reflectometers are built for small divergences (up to $\approx 0.4^\circ$) and use the approach of defining the beam using a pair of slits (often this is referred to as *focusing*, but slits just cut down the phase space, they do not spatially concentrate flux). This restricts the possible gain factors and the wide opening of the slits necessary for high-intensity specular reflectometry leads to a strong illumination of the sample environment and thus to high background. Thus one needs some optics to deliver a truly focused beam in a sense that only a defined small spot is illuminated and, ideally, not the surrounding area.

[1] A periodic multilayer, normally referred to as *monochromator coating*. This term is not appropriate here because in total a wide wavelength band is reflected.

2.1. The Selene guide

Over recent years we have developed a truly focusing neutron guide system which we called *Selene* guide [4,5]. This attempt was triggered by ideas of Ott [3,6]. Later we found that in 1963 a similar guide was suggested by Maier Leibnitz and Springer [7], but at that time it could not be realised technically. The initial intention was to use it for reflectometry as is described here, but it can also be applied to other purposes as long as the guide length, the wavelength range, the sample size and the requested divergence are within limits imposed by gravity and the available (and affordable) coating of the guides.

This *Selene* guide system is made of two subsequent planar-elliptical reflectors which share the long axis and one focal point. This leads to an imaging system where coma aberration, which is inherent to elliptical mirrors, is corrected to first order. This means that the geometrical properties of the beam at the final focal point (in the presented case the sample position) can be defined at the initial focal point, here referred to as the *virtual source*. When this concept is applied in the horizontal and vertical direction normal to the beam, a 3-dimensional image of the virtual source is projected onto the sample. Fig. 1 illustrates this geometry.

Used for reflectometry, the imaging property means that the beam-footprint on the sample surface is defined a long distance away from the sample. This leaves more flexibility for the sample environment. The maximum divergence of the beam is defined by the emittance of the virtual source and the geometry of the guide. It can be reduced in a defined way by using an aperture at the exit of the guide, still far from the sample. The restriction of the divergence does not affect the footprint, and vice versa.

The *Selene* guide is not to be confused with 4-sided elliptic neutron guides. Those typically have their entrance and exit quite close to the focal points, and they are used on large sources. As a consequence aberration leads to garland and zigzag trajectories in the guide and the geometrically focusing property is largely lost.

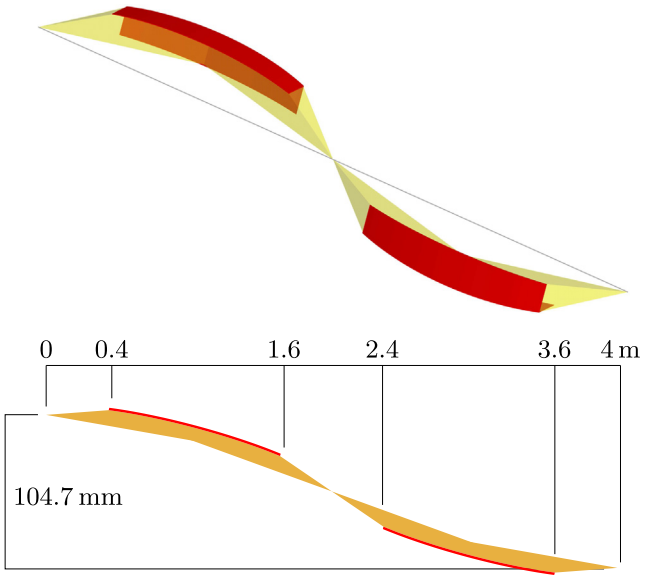

Fig. 1. Illustration of the geometry of a *Selene* guide. The first pair of planar elliptic mirrors (red), mounted at 90°, focuses the neutron beam (yellow) to the intermediate focal point. At this point the beam is strongly affected by coma aberration. The second pair, oriented opposite to the first pair, reverses the aberration and leads to a sharp true sided image of any small (virtual) source at the initial focal point. Thus unlike *normal* neutron guides, even elliptic ones, the *Selene* guide does not have a rectangular cross-section, but is open with an L-shape. (For interpretation of the references to color in this figure caption, the reader is referred to the web version of this paper.)

Only a small fraction of the transported neutrons are actually focused [8] and the beam leaving these guides is divergent right behind the exit. However, an adequate design can lead to an intensity concentration on a relatively small area [9,10]. These elliptic guides allow larger beam cross-sections, wider divergence and they show less (if any) chromatic effects. The prize one has to pay is that the sample is strongly over-illuminated. Stopping all the unwanted neutrons (more than 99%) by absorbers behind the guide exit and before the sample leads likely to a high background and to radiation issues.

3. *Selene* guide as an add-on for Amor

3.1. The demonstrator

Full-scale *Selene* neutron guides (from source to sample) were discussed for a potential guide upgrade at PSI and for various instruments at the European Spallation Source (ESS) under construction in Sweden. To validate the concept and to learn about alignment and measurement procedures we constructed a down-scaled demonstrator of the *Selene* guide. The actual dimensions and the resulting performance of the guide as given in Table 1 were obtained by optimisation to the space and wavelengths available at the test beamline BOA at PSI.

The demonstrator was developed at PSI, fabrication including coating was performed by SwissNeutronics.

After some initial tests on BOA, the guide support was strongly simplified and the full guide was mounted on one aluminium beam with the possibility to vary horizontal and vertical inclination. This allowed us to continue the tests on the TOF reflectometer Amor at PSI (see below). The results encouraged us to modify Amor and to construct a spin polariser and an RF flipper, so that the demonstrator can be used as an add-on for user operation.

3.2. The TOF-reflectometer Amor

Amor was built as a very flexible reflectometer which optionally allows for measurements on liquid surfaces [11]. As it is hosted at a continuous neutron source (SINQ is a spallation neutron source with a frequency of 50 MHz) a pair of choppers is installed right after the neutron guide exit. This allows for a constant σ_λ/λ operation [12].

Besides a slit behind the chopper housing and the frame-overlap mirror, all optical and mechanical components are mounted on an 8 m long granite block, acting as an optical bench. In the conventional setting these components are (along the beam): reflecting polariser or deflector/slit 2/horizontally focusing parabolic guide segment[2]/slit 3/sample stage/slit 4/analyser/and slit 5 in front of the detector. The detector (optionally 0- or 2-dimensional) is mounted in a way that its composite movement (inclination, horizontal and vertical translation) describes an arc around the sample position.

With this set-up one can reach a q_z-range up to 0.3 $Å^{-1}$ (limited by the maximum detector angle). The resolution can be tuned, but in almost all cases $\sigma_{q_z}/q_z \approx 4\%$ is chosen.

The area-sensitive wire detector has an active area of 180 × 180 mm^2 The intrinsic spatial resolution is $\sigma_z \approx 1.2$ mm, but the data are binned with 128 × 256 channels. Each event is discretized into a (t, y, z) channel and counted in a histogram memory. Only after the measurement the data array is transferred to the computer, stored in the nexus format [13] and available for further processing. The storing process takes 6–10 s.

3.3. Modifications

The use of the demonstrator guide on Amor was restricted by the fact that a *Selene* guide causes a parallel offset of the beam, both horizontally and vertically. The vertical offset could be realised by translation stages which are otherwise used to measure with an inclined beam. But for the horizontal offset of 104.7 mm, the granite block had to be mounted on a motorised translation system so that a fast switching between the normal operation geometry and the *Selene* add-on is possible.

For the time being, the first slit directly behind the chopper housing, is used as virtual source. The subsequent components up to slit 3 have to be removed to provide space for the *Selene* guide. Thus an other way to polarise and flip the beam had to be implemented.

3.4. Constraints

The geometry of Amor and the beam characteristics at the end of the guide feeding the chopper impose some constraints. Slit 1 is located 1600 mm from the end of the guide, which has a cross-section of 50 × 50 mm^2. Thus the maximum divergence after the virtual source is 1.8°, which just illuminates the *Selene* guide. In addition, beams with a high angle relative to the Amor guide axis did undergo multiple reflections (up to 8 vertically and up to 17 horizontally due to the split guide geometry) and are thus of lower intensity.

The coating of the Amor guide is of $m=2$, which means that the full 1.8° divergence is obtained for $\lambda > 3.8$ Å, which matches the *Selene* guide's acceptance of 4 Å.

The area detector has a spatial resolution of $2\sigma_z \approx 2.5$ mm. To still obtain a high angular resolution, the detector is moved as far back on the optical bench as possible, i.e. ≈4 m from the sample. This results in a relatively high wavelength resolution $\sigma_\lambda/\lambda \approx 2.3\%$. To avoid frame overlap due to the longer flight path, the chopper frequency has to be reduced to 33 Hz (instead of the normal 50 Hz).

The *Selene* guide can accept neutrons from a region of ≈2 × 2 mm^2 in the plane of the virtual source. Thus the maximum footprint width on the sample is only 2 mm.

3.5. Optics

3.5.1. Polariser

A new type of polariser was designed for the *Selene* set-up on Amor, which makes use of the facts that the beam to be polarised originates from a small area and that far from the origin it has locally a small divergence.

We choose a supermirror-based polariser operated in transmission. To ensure the same angle of incidence for all beam trajectories, the polariser is bent to form a logarithmic spiral

Table 1
Basic geometrical parameters and derived properties of the demonstrator guide.

Source-sample distance	$4c$	4000 mm
Half-axes ratio	b/a	0.021480
Normalised length	ξ	0.60
Divergence	$\Delta\theta$	1.8° × 1.8°
Horizontal and vertical inclination	$\epsilon_{y,z}$	1.50°
Parallel offset		104.7 mm
Maximum spot size	$\Delta y \times \Delta z$	2 × 2 mm^2
Coating	m	2.5
Critical wavelength	$\lambda_{\min}$	4 Å

[2] This focusing guide concentrates the flux onto a 10 mm wide spot with 3 times the unfocused intensity.

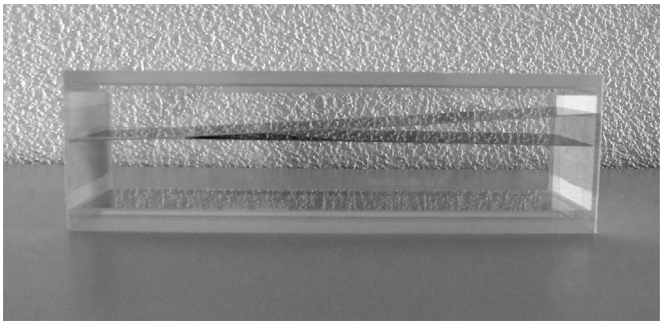

Fig. 2. Photo of the polariser and frame-overlap mirror based on transmission through equiangularly curved coatings. The glass tube is 215 mm long and has an inner height and width of 50 × 50 mm^2. The virtual source is to be 170 mm before the entrance (to the left). The device was produced by SwissNeutronics.

(equiangular spiral) with its pole at the beam origin. Since the *Selene* guide already starts 400 mm behind the virtual source, the space is rather limited, so that the actual polariser consists of two spirals with opposite sense of curvature, forming a V-shape. The coating, an $m=4.2$ Fe/Si supermirror, is applied to both sides of the substrates, 40 mm wide and 240 mm long Si-wavers. The spiral shape is defined by corresponding grooves in the inner sides of the rectangular glass-tube used as housing (see Fig. 2). To ensure a high polarisation efficiency, the device is mounted within a magnetic field of $H=400$ Oe, realised with permanent magnets.

The spin can be flipped with an RF flipper positioned behind the first guide segment.

3.5.2. Virtual source

Since the *Selene* guide acts as a 3-dimensional imaging optics, one can back-project the required beam footprint on the sample to the virtual source position. A diaphragm (an assembly of absorbing blades) with the shape, size and orientation of this projection is used at this position to define a *luminous field* being mapped to the sample.[3] For a perfectly aligned aperture and *Selene* guide only slight distortions occur due to gravitational aberration and remainders of coma aberration. No further optics is needed in this case.

The reality is that our first version of a luminous-field diaphragm is not precise and reliable enough, thus it is not used at present. A new device is being planned.

3.6. Set-up

Fig. 3 shows a CAD image of Amor with the *Selene* guide installed. The complete guide is mounted on an aluminium beam, which is hosted on a carriage on the optical bench. This and all the following components can be positioned along the instrument axis individually.

It is worth noting that there is a relatively wide free space around the sample as the guide ends 400 mm up stream. The motorised (bulky) slit 3 can be replaced for a thin fixed slit (if needed at all) and thus sample environment with a radius of 390 mm can be used. This is enough for a horizontal 7 T magnet or a sputter chamber for in-situ sample preparation.

3.6.1. Alignment of the Selene guide

For the alignment of the individual reflectors (in total 8 with a length of 600 mm, each) relative to each other, and of the full guide on the optical bench of Amor, we use optical light. Up to now

[3] In optical microscopy the analogue is called luminous-field diaphragm, field diaphragm or (if quasi circular) iris diaphragm. We adapted the first term since it illustrates best the purpose of the device.

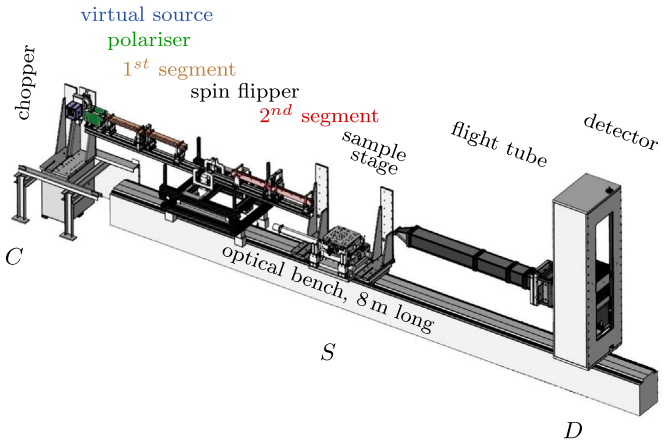

Fig. 3. CAD image of Amor showing the set-up with the *Selene* guide, the related optics, and the flight tube in front of the detector. *C*, *S* and *D* indicate the locations of the chopper, the sample and the detector, respectively.

white light is provided by an LED spotlight. A pinhole of 0.5 mm diameter defines the initial focal point. The reflector elements are then mounted and adjusted one-by-one in a way that the light emerging from the pin-hole is focused to the intermediate or final focal points, respectively. Even tiny deviations of the alignment lead to a broadening of the spots in the focal plane, or to a stripe-pattern of the spot on a screen before or behind the focal planes.

The orientation of the horizontally and vertically reflecting elements relative to each other should be 90°. This can be checked by looking at the joint of both: the double-reflected image of ones pupil should be round. Any compressed or elongated shape is a result of a too large or small angle, respectively. The 90° alignment leads to the diagonal dark line in the $I(y,z)$ map shown in Fig. 4. Besides some imperfections of the mirrors along the joint, this is caused by the parallaxes error the first reflection on the guide element introduces for the second reflection [14]. An optimisation of the angle is possible for short devices (relative to the focal point distance) as with Montel optics used at synchrotron beamlines. For long devices the optimisation in the entrance region is in conflict with the optimisation of the exit region.

With this alignment method a beam-spot size at the sample position below 1 mm in diameter can be reached. For the near future it is foreseen to replace the LED/pin-hole arrangement by a LASER/optics set-up creating a virtual point source in the μm−range. The screens will be replaced by an assembly of a

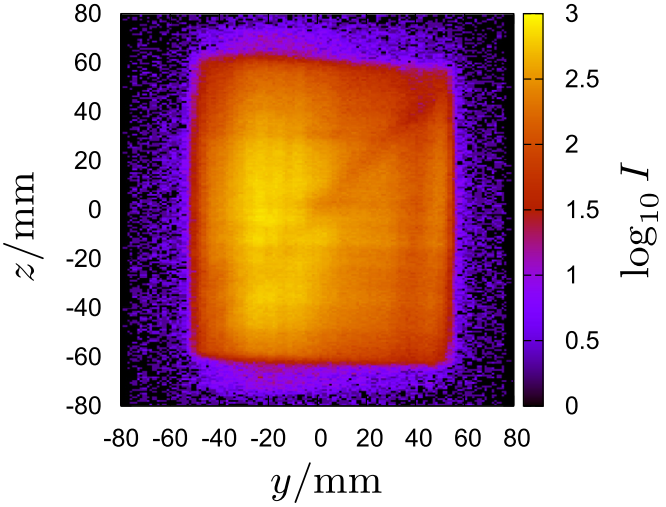

Fig. 4. Intensity map of the direct beam (without sample, $\gamma_D=0°$) on the detector, integrated over all wavelengths.

refraction-free beam splitter and two cameras in the focal plane and 15 cm behind it, respectively.

3.7. Limitations and areas of application

At the moment there is no spin analyser available for the focusing beam set-up on Amor. Thus spin-flip scattering cannot be investigated.

The present polariser (see Section 3.5) also acts as frame-overlap filter. For unpolarised measurements this means that there is no filtering of long wavelengths, which might lead to increased background at short wavelengths, i.e. high q_z. In the experiments performed so far this was not of relevance.

The *Selene* guide transports only neutrons coming from the close vicinity of the initial focal point. This has the effect that the maximum width of the footprint on the sample is only about 2 mm wide. Without the luminous-field diaphragm the maximum length of the footprint is restricted to 2 mm/ $\tan\theta$. With down to 24 mm this exceeds most of the samples measured on Amor even for highest possible θ.

The maximum detector angle γ_D of Amor is 8°, and the minimum wavelength transported by the *Selene* guide is 4 Å. This leads to an upper limit of $q_z \approx 0.23$ Å^{-1}.

The beam reaches the sample position horizontally. Measurements on liquid/liquid or liquid/gas interfaces are thus not possible in the standard configuration. A reflector behind the guide exit to bend down (or up) the beam is not yet realised.

Positively phrased, the *Selene* set-up works best for solid state samples with a small surface area, or where only a restricted area should be illuminated. For typical samples of 10 mm width the counting time is reduced by a factor 5 compared to the normal set-up on Amor already using a horizontal focusing.

The relatively short counting times together with the space around the sample enable time-resolved in-situ or in-operando studies. The highest time resolution reached up to now was about 1 min to cover $q_z \in [0.005, 0.07]$ Å^{-1}. Prominent reflectivity peaks at low q_z would allow for even shorter counting times.

4. Data acquisition and reduction

4.1. Sample alignment

Fig. 5 shows the geometrical situation at the sample in the scattering plane together with the nomenclature used here.

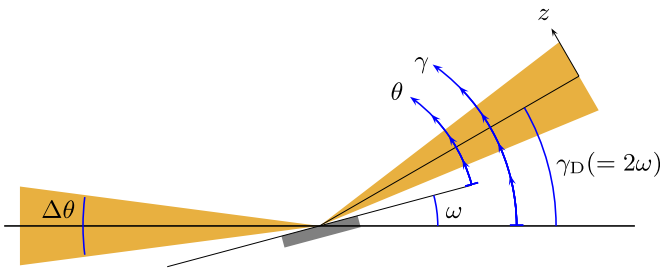

Fig. 5. Sketch of the sample geometry in the scattering plane. The yellow area shows the incoming and reflected beam, both with the divergence $\Delta\theta$. The inclination of the sample relative to the centre of the incoming beam (here identical to the instrument horizon) is called ω, and the respective angle of the reflected beam relative to the same axis is γ. In general the detector centre is located at $\gamma_D = 2\omega$. These are *instrument coordinates* and should not be confused with the situation on the sample, where the take-off angle of an individual neutron trajectory is called θ. While related to the instrument settings (see Fig. 6 (g)), this is the only relevant angle for data analysis. (For interpretation of the references to color in this figure caption, the reader is referred to the web version of this paper.)

Neither ω nor 2θ are well defined with a convergent beam anymore and thus *new* angles and definitions are introduced.

The focusing of the beam leads to an unfamiliar behaviour: As long as the sample surface is in the beam, the total reflection plateau will show up as a triangle in the $I(\lambda,\theta)$ map (see Fig. 7(j)), even for an angular misalignment of up to 1°. The challenge is to bring the sample to the focal point with an accuracy better than 0.1 mm.

Whenever possible we use white light coupled into the neutron beam path to actually see the focal spot. In these cases it is also possible to roughly align $\omega = \gamma_D/2$ by looking for the light reflected off the sample. In other cases one has to scan the sample through the beam until the mentioned triangle shows up. Probably this has to be repeated with a different ω, where the steps in ω are of the order of 0.5°.

Once one gets the wanted signal in $I(\lambda,\theta)$, one can precisely adjust ω. It is correct, when the inclined side of the triangle, which corresponds to the critical q_z, points to the origin ($\lambda = 0$ Å, $\theta = 0°$). In the final step the sample is scanned through the focal spot to find the best (most intense and homogeneous) illumination.

Our experience is that a misaligned ω can be easily corrected for after the measurements, but a shifted sample requires an equally shifted reference (see below) to ensure a correct data reduction.

The alignment normally is performed at a detector position of $\gamma_D = 2.2°$ and $\omega \approx 1.1°$ where there is no overlap with the non-reflected beam but still relatively high intensity due to the small q_z.

4.2. Measurement

For the measurement the required q_z-range determines the ω and $\gamma_D (= 2\omega)$ settings. Taking the actual λ- and θ-dependence of the incoming beam on Amor into account one can estimate the sample inclination based on the lower q_z limit with $\omega \approx 0.9° + \arcsin q_l \cdot 0.95$ Å and the corresponding upper q_z limit is then $q_u \approx 2.8 q_l + 0.09$ Å^{-1}. For most applications the angles $\omega = 1.1°$ and 3.6° are sufficient to cover $q_z \in [0.004, 0.23]$ Å^{-1}.

The counting times vary between a minute for relatively large samples (40 mm long) and time-resolved studies at small q_z, and several hours for samples of 5 mm length and $q_z \in [0.005, 0.23]$ Å^{-1}.

Each measurement results in a histogram $\mathbf{H}_{raw}$ with entries $H_{raw\ ijk}$ = counts in time interval i and detector pixel jk, the one-dimensional arrays for time $\mathbf{t}$ and the detector coordinates $\mathbf{z}$ and $\mathbf{y}$, and the monitor signal n_{mon}. The latter replaces the counting time because the neutron beam flux at SINQ is not constant, but changes on a split-second time-scale. Thus the beam intensity before the chopper is monitored. So the intensities $I = H/n_{mon}$ discussed below are of the dimension counts per monitor signal, rather than counts per second.

4.2.1. Reference

To reduce and to normalise $\mathbf{H}_{raw}$ a known reference sample is used, measured under similar conditions. Ideally this reference has the same dimensions as the sample and a high reflectivity. We use an $m = 5$ Ni/Ti supermirror[4] (SM) with a known reflectivity $R^{SM}(q_z)$. It is measured at $\omega \approx 1.1°$ ($\mathbf{H}^{SM}$) and at 3°. The first angle ensures that the full λ-θ-range corresponds to a $q_z < q_z^{c,SM}$, the second measurement showing the critical edge $q_z^{c,SM}$ is used to cross-check ω.

[4] The number m relates the critical q_z of the supermirror to that of natural Ni.

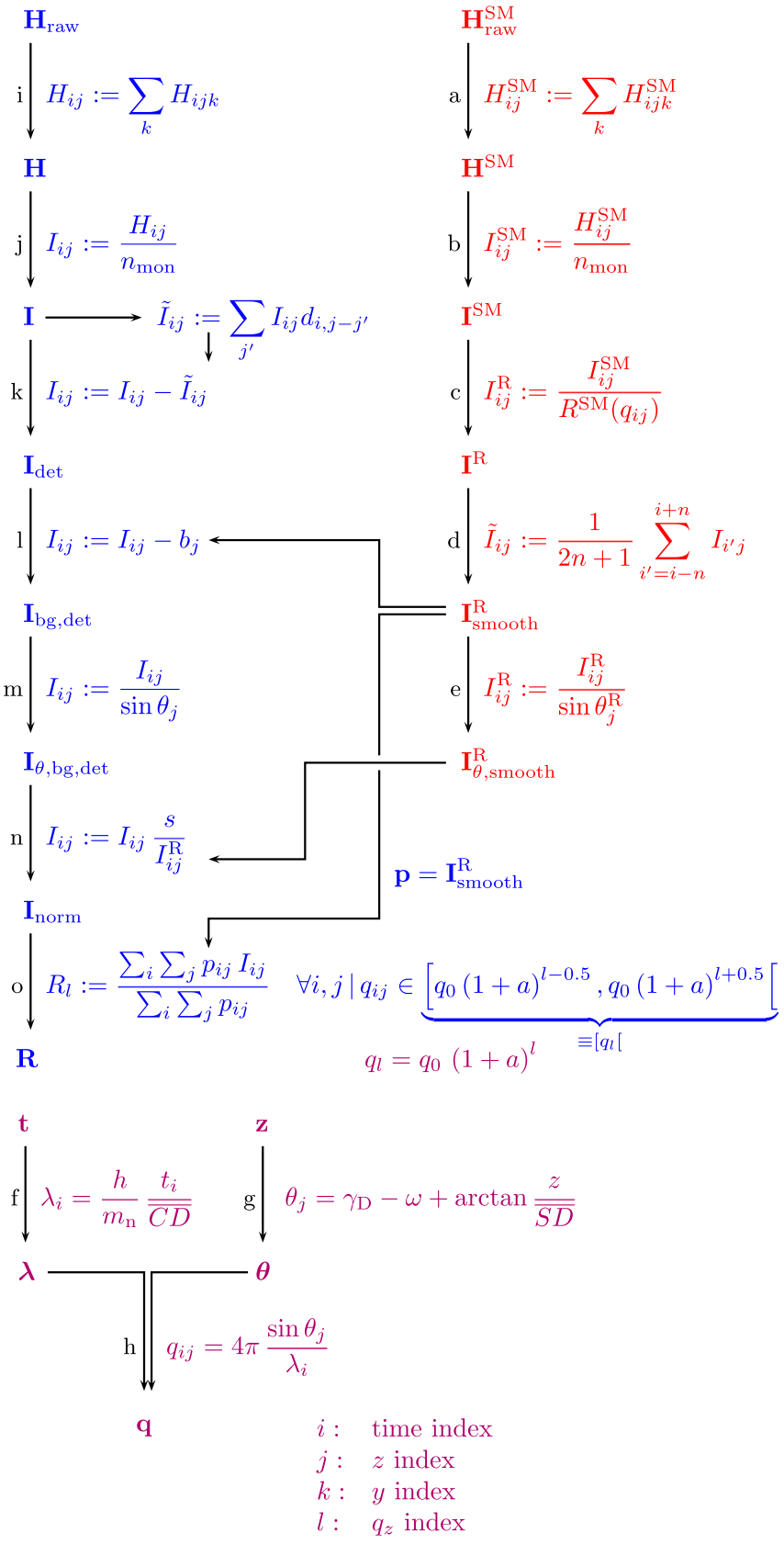

Fig. 6. Flow chart (simplified) of the data reduction process. The first column (blue) corresponds to the sample measurement, here **H** means histogram, **I** means intensity and **R** reflectivity. Bold symbols stand for data arrays, where the array elements have the indices i,j,k and l, referring to time, detector z coordinate, detector y coordinate and q-bin, respectively. The second column (red) corresponds to the reduction of the supermirror measurement ($^{\mathrm{SM}}$) to obtain the reference ($^{\mathrm{R}}$). On the right the connection of the histogrammed time- and position-data and the parameters wavelength λ and reflection angle θ and finally momentum transfer q are given. The first row contains the raw data stored in the measurement file. The small letters refer to the related entries in the text. (For interpretation of the references to color in this figure caption, the reader is referred to the web version of this paper.)

4.3. Data reduction

To obtain the reflectivity $R(q_z)$ (or more precise the one-dimensional reflectivity array **R**) from the measured histogram **H** the latter has to be corrected for influences of the scattering geometry and the intensity distribution of the incoming beam. In addition, background originating from the instrument and its environment can be subtracted.

In this section the essential data reduction steps are discussed briefly. Fig. 6 shows a simplified flow chart of the reduction process. The correction is indicated by a subscript. In parallel to the shown steps, a full error handling is performed.

Fig. 7 shows intensity maps for some of the data arrays obtained during the reduction and the final reflectivity for the example presented in Section 5.

4.3.1. Reference

The reference measurement data enter the reduction process in three different ways: it gives an estimate for the background **b**, allows for the normalisation of the intensity array **I** and delivers the weighting factors **p** for the projection of the latter onto a q_z-grid.

The reduction process for the reference is summarised in the second column of Fig. 6. It essentially consists of

(a) Projection of the three-dimensional histogram $\mathbf{H}^{\mathrm{SM}}_{\mathrm{raw}}$ onto the two-dimensional $\mathbf{H}^{\mathrm{SM}}$.
(b) Normalisation by the monitor counts n_{mon} to get the intensity array $\mathbf{I}^{\mathrm{SM}}$.
(c) Normalisation by the reflectivity of the supermirror $R^{\mathrm{SM}}(q)$ resulting in the total intensity incident on the reference $\mathbf{I}^{\mathrm{R}}$.
(d) Smoothing along the time coordinate to reduce the statistical noise. This is justified by the expected smoothness of R^{SM} below the critical edge and of the neutron spectrum.
(e) Illumination correction, taking into account the sample size projected onto the detector (see Fig. 7(e)).

For some correction steps the wavelength, the reflection angle or q_z are needed. The respective formulae are given in the right part of Fig. 6:

(f) Calculation of the wavelength from the histogramming time-steps **t** using the chopper-detector distance $\overline{CD}$, the Planck constant h and the neutron mass m_{n}.
(g) Calculation of the reflection angle θ from the detector angle γ_{D}, the sample orientation ω, the sample-detector distance $\overline{SD}$ and the z-position on the detector.
(h) Association of a q_z with each bin, resulting in a two-dimensional array **q**.

4.3.2. Sample

The first reduction steps for the sample are similar to the ones for the reference. The essential steps are displayed in the first column in Fig. 6.

(i) Projection of the three-dimensional histogram $\mathbf{H}_{\mathrm{raw}}$ onto the two-dimensional **H**.
(j) Normalisation by the sample monitor counts n_{mon} to give the intensity array **I** (see Fig. 7(j)).
(k) Correction of the spatial detector response function. The Al window of the detector scatters a fraction of the incoming neutrons and thus leads to a halo decreasing exponentially with distance r around each irradiated point [15, Fig. 10 and discussion]. In principle $\mathbf{H}_{\mathrm{raw}}$ has to be deconvoluted with a λ-dependent response function. We chose the simplified approach to subtract the measured array **I** convoluted with d

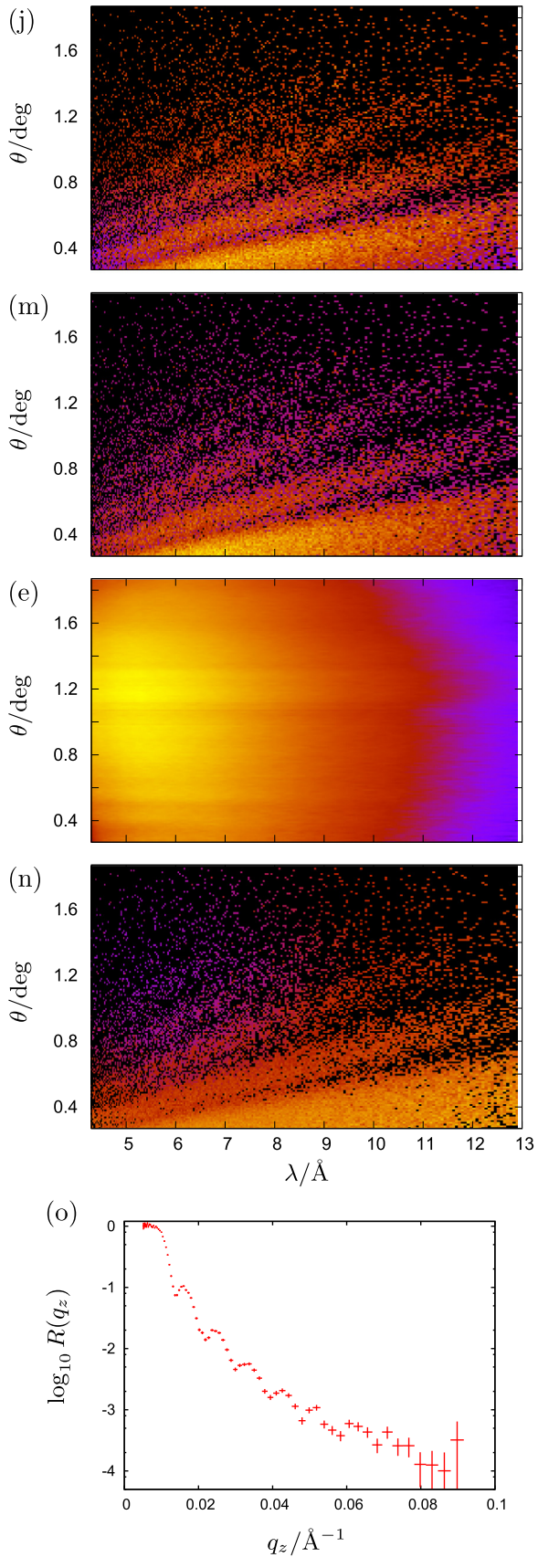

Fig. 7. Illustration of the essential reduction steps. The numbering corresponds to the one in the text and in Fig. 6. (j) intensity as detected (**I**) and (m) after θ-correction ($\mathbf{I}_{\theta,\mathrm{bg,det}}$). (e) θ-corrected reference measurement. (n) reflectivity $\mathbf{I}_{\mathrm{norm}}$. (o) reflectivity **R** after projection onto a q_z grid.

(λ, z) describing the wings of response function. $d(\lambda, z)$ was obtained from fits to measurements.

The difference between the two blue lines in Fig. 11(a) tells the order of magnitude of this correction.

(l) Background subtraction. Background coming from the sample or (in the case of over-illumination) from its environment due to incoherent scattering has the time-characteristics of the incident beam, but only a weak θ dependence. To estimate the background $b(\lambda)$ the reference measurement is summed over θ and scaled with a factor b':

$$b_j = b' \sum_i I^{\mathrm{R}}_{ij} + b''$$

b' and a time-independent contribution b'' (due to external sources or activated components) can be determined e.g. by measurements with $\omega < \gamma_{\mathrm{D}}/2 - \Delta\theta/2$, or by fitting.

(m) Illumination correction analogue to (e), but probably with a different $\boldsymbol{\theta}$ (see Fig. 7(m)).

(n) Normalisation to the wavelength-dependent flux incident on the sample. This is achieved via pixel-by-pixel normalisation of $\mathbf{I}_{\theta,\mathrm{bg,det}}$ with $\mathbf{I}^{\mathrm{R}}_{\theta,\mathrm{smooth}}$. A scaling factor s takes differences of sample and reference size into account and it can correct for the unstable monitor efficiency on Amor[5] (see Fig. 7(n)).

(o) In the last step the two-dimensional reflectivity array $\mathbf{I}_{\mathrm{norm}}$ is projected onto a defined q_z-grid. By default a logarithmic grid is used with a resolution of $q_{l=0} = 2e^{-3}$ Å^{-1}. The weighting factors for the summation are the entries of the reference array $\mathbf{I}^{\mathrm{R}}_{\mathrm{smooth}}$ before the illumination correction. The reason is that otherwise the low-θ region with relatively low statistics (due to the small angle of incidence) would be overemphasised.

Steps (e), (m), (n) and (o) can be summarised as

$$R_l := \frac{\sum_{ij} \frac{\sin\theta^{\mathrm{R}}_j}{\sin\theta_j} I_{\mathrm{bg,det}\ ij}}{\sum_{ij} I^{\mathrm{R}}_{\mathrm{smooth}\ ij}} \quad \forall i,j \mid q_{ij} \in [q_l[\tag{1}$$

4.3.3. Resolution

The problem with the approach to sum over equal q_z intervals (Fig. 6(o)) is that the resolution varies over $\mathbf{I}_{\mathrm{norm}}$.

The wavelength resolution is given by the double-blind chopper system [12] of Amor and its distance to the detector. The pulse has an almost rectangular shape. For the *Selene* set-up one gets $\Delta\lambda/\lambda = \overline{C_1C_2}/\overline{CD} \approx 5.8\%$, here. $\overline{C_1C_2} = 490$ mm is the distance between the first and second chopper disks. This corresponds to $\sigma_\lambda/\lambda \approx 2.3\%$.

The angular resolution is given by the spatial resolution of the detector with FWHM $\Delta z \approx 2.5$ mm and the sample-detector distance $\overline{SD} \approx 4$ m:

$$\sigma_\gamma = \frac{1}{2\sqrt{2\ln 2}} \arctan\frac{\Delta z}{\overline{SD}} \approx 0.016^\circ \tag{2}$$

For larger samples (length x_{S}) and high angles the projected size of the footprint might be of the same order or larger than the detector resolution. This leads to

$$\sigma_{\theta\, j} = \sqrt{\sigma_\gamma^2 + \left(\frac{1}{2\sqrt{2\ln 2}} \arctan\frac{x_{\mathrm{S}} \sin\theta_j}{\overline{SD}}\right)^2} \tag{3}$$

The resulting q_z-resolution is

$$\frac{\sigma_{qij}}{q_{ij}} \approx \sqrt{\left(\frac{\sigma_{\lambda\, i}}{\lambda_i}\right)^2 + \left(\frac{\sigma_\gamma}{\theta_j}\right)^2 + 0.18\left(\frac{x_{\mathrm{S}}}{\overline{SD}}\right)^2} \tag{4}$$

[5] The monitor efficiency on Amor varies by up to 10% on a time scale of several hours.

Fig. 8 shows calculated σ_q/q_z curves as a function of θ. While the sample size has only a minor influence, the detector resolution spoils the q_z-resolution for small θ. Taking this into account, the measurements should be performed at an ω as high as possible, but still covering the interesting q_z-range. Optionally one can evaluate the scaling factor s from total reflection by using the full θ-range, and then repeat the summation with a reduced range to get higher resolution.

The q_z resolution for each entry in the reflectivity array $\mathbf{R}$ is obtained analogue to step o in Fig. 6:

$$\sigma_{q_l} := \frac{\sum_{ij} p_{ij}\, \sigma_{q\ ij}}{\sum_{ij} p_{ij}} \quad \forall i,j \mid q_{ij} \in [q_l] \tag{5}$$

Fig. 11 illustrates the validity of these considerations by comparing measured data to simulations taking into account only the wavelength resolution or the resolution obtained by Eq. (5).

In the case of a curved sample surface the reflection for each incoming θ gets blurred on the detector, which might dominate the resolution and render a useful data analysis impossible. In this case the wide divergence provided by the *Selene* guide cannot be used, but must be restricted with slits at the guide exit.

R. Cubitt recently published a similar approach for data reduction for cases when the detector is used to determine θ [16]. The essential difference is that there a flat $I(\theta)$ distribution over the incoming beam is assumed and no reference sample is used.

5. Example: in-situ annealing

The example of in-situ annealing for the investigation of Li diffusion in Si is used here to illustrate some of the reduction steps discussed above and the performance of the *Selene* guide. The data are courtesy of E. Hüger and H. Schmidt, Technical University of Clausthal, Germany.

This experiment was chosen because the required time-resolution and the measurement time on Amor match. These measurements [17] were performed with an unpolarised beam. The counting time per reflectivity reached down to 90 s. A special annealing chamber based on the system AO 500 by MBE Komponenten was build to fit on the sample stage of Amor (see Fig. 9).

The samples were multilayers of the type ^{6}LiNbO$_3$/[Si/^{7}LiNbO$_3$/Si/^{6}LiNbO$_3$]$_5$/Si with equal thicknesses of the respective

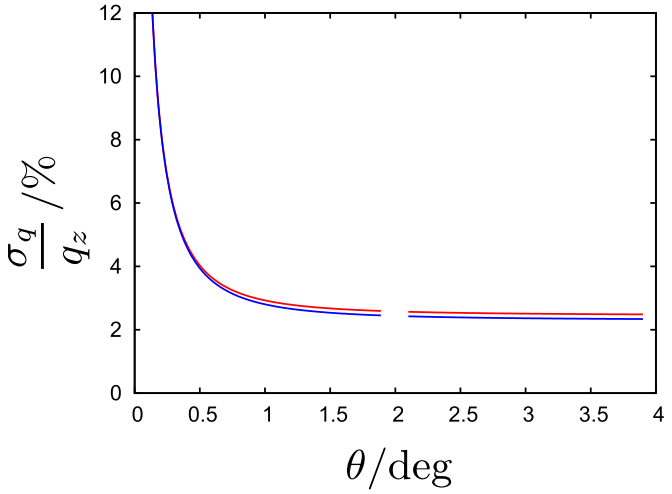

Fig. 8. Resolution σ_{q_z}/q_z as a function of θ for sample length of l=40 mm (red curves) and 10 mm (blue curves), respectively. A wavelength resolution of σ_λ/λ = 2% was assumed and a sample-detector distance $\overline{SD} = 4$ m. The curves correspond to ω=1° and 3°, respectively. (For interpretation of the references to color in this figure caption, the reader is referred to the web version of this paper.)

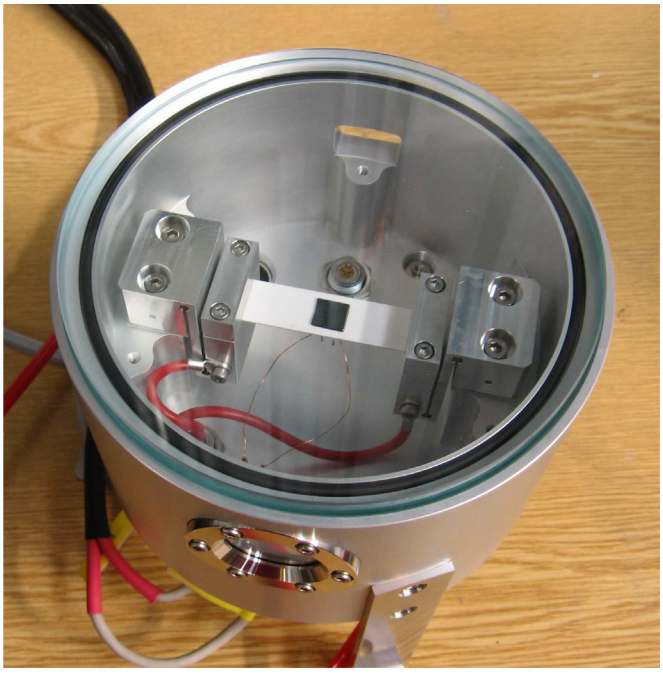

Fig. 9. Furnace for in-situ/in-operando annealing. The beam enters and leaves the recipient through sapphire windows. The 1 cm^2 sample is visible as a dark square on the white resistive heater bar.

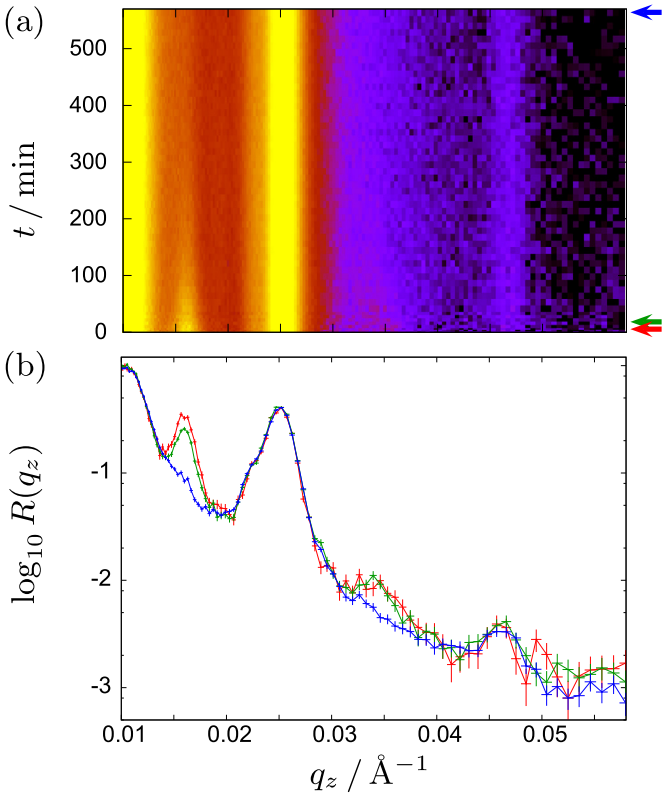

Fig. 10. (a) Intensity map $R(q_z)$ as a function of annealing time (in minutes) for a multilayer of $[^6Li_3NbO_4/Si/^7Li_3NbO_4/Si]_5/Si$. The colour scale is non-linear and was adapted to highlight the interesting features. (b) Selected $R(q_z)$ curves from this map measured at $t=0\rightarrow3$ min (red), $t=18\rightarrow24$ min (green) and $t=558\rightarrow570$ min (blue). (For interpretation of the references to color in this figure caption, the reader is referred to the web version of this paper.)

Si or $LiNbO_3$ layers [18,19]. The strong contrast at the chemical interfaces leads to a pronounced Bragg peak in the reflectivity curve. The contrast between the two Li-containing layers is much weaker. The doubled period results in a small Bragg peak in between the total reflectivity plateau and chemical Bragg peak. Upon annealing the diffusivity of Li through Si is increased, which leads to an assimilation of the $^6Li/^7Li$ ratios and thus to a decrease of the corresponding Bragg peak. The lithium permeability (solubility × diffusivity) describing the transport through the silicon layer can be derived from the Bragg peak decrease [17–19]. From the temperature (in the range 80–380 °C) and the measured time constant of the decrease (6–60 min) one can extract the activation energy of the mobility of Li in Si.

For the actual measurement the sample was mounted and aligned, then a reflectivity measurement was performed before annealing and then every 90 s during annealing. I.e. the sample was not cooled down for measurements.

Fig. 10 shows a typical intensity map of $R(q_z)$ vs. q_z and annealing time t for these kind of measurements, together with some selected $R(q_z)$ curves. The decrease of the Bragg peak associated with the isotope contrast (at $q_z \approx 0.16$ Å^{-1} and higher orders at 0.34 Å^{-1} and 0.57 Å^{-1}) is nicely visible. The chemical Bragg peaks stay unchanged.

On an other sample of similar composition a series of measurements have been performed with much better statistics in order to illustrate some of the aspects discussed in Section 4.3. Fig. 11(a) shows the reflectivity curves for $\omega=1.0°$ with and without the correction for the detector response function, the simulated reflectivity taking only the wavelength resolution into account and the resolution σ_q/q obtained from the experimental data using Eq. (5). It is obvious that ignoring the detector resolution in the simulated data leads to a wrong result for $q_z < 0.04$ Å^{-1}. The red lines in Fig. 11(b) and (c) are the simulated reflectivity convoluted with a Gaussian function using the experimental $\sigma_q(q)$ displayed in (c). The experimental data collected at $\omega=3.0°$, shown in (b), were merged with the ones in (a) to give the curves shown in (c).

6. Outlook

For the near future we plan to improve the alignment procedure for the *Selene* guide and for the sample, respectively. The latter involves sample environment that allows for a better access to the sample and for a reliable and stable sample position.

A spin analyser also based on the equiangular spiral concept is in planning.

The resolution issue for small θ and the time loss during data download from the histogram memory can be solved with a detector with higher spatial resolution in the scattering direction $\Delta z < 0.5$ mm and faster electronics (integral count rate 10^4 s^{-1} for the demonstrator, $>10^5$ s^{-1} for a full scale guide allowing for larger footprints).

On the longer time scale the complete guide feeding Amor might be replaced by a *Selene*–type guide. Depending on the spatial constraints either the moderator or a pin-hole several meters downstream of it will form the initial focal point. The final focal point again defines the sample position. The granite beam will have to be moved towards the moderator by several meters and tilted. Fig. 12 shows sketches of the present and the planned guide layout. Assuming the divergence and transmission of the full guide to be the same as of the demonstrator, the gain is given by the omission of the old guide with its low transmission (only 20%) and inhomogeneous phase space (due to many reflections for

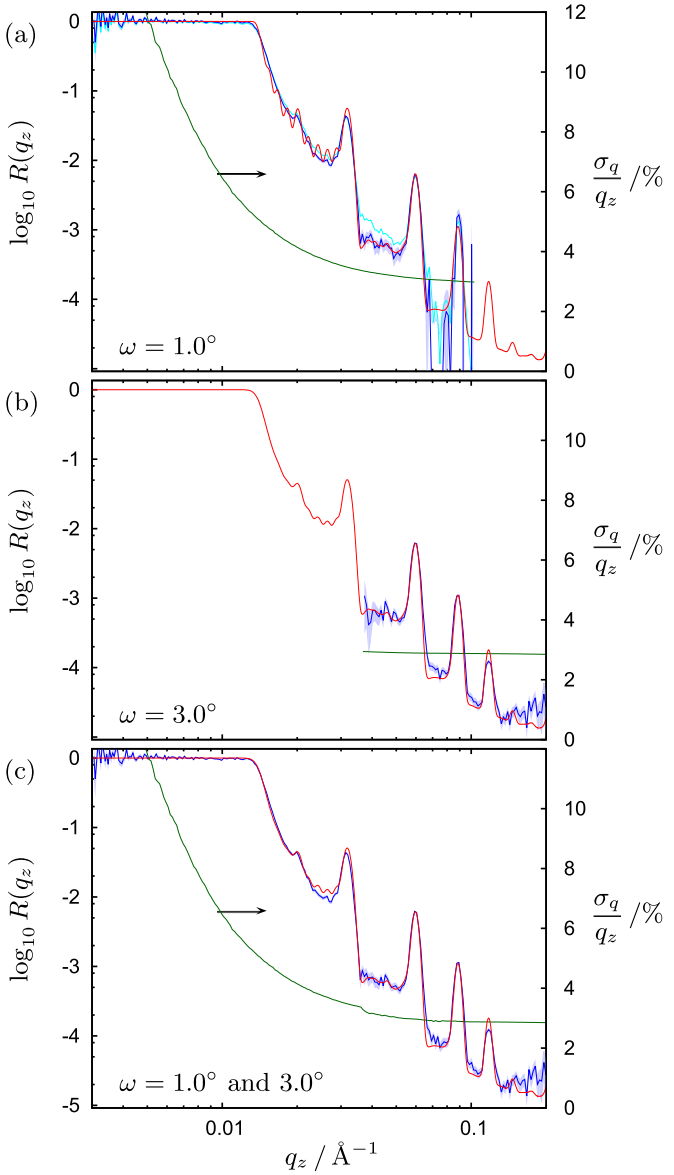

Fig. 11. Measured (blue with a pale blue error region) and simulated (red) reflectivities for a $LiNbO_3$/Si multilayer (after annealing) as discussed in Section 5. The green lines show the resolution σ_q/q_z and are related to the second y-axis. (a) Data set obtained at $\omega = 1.0°$ with (dark blue) and without (light blue, no error region) correction for detector response are discussed in Section 4.3.2(k). Simulated data convoluted with $\sigma_q/q = \sigma_\lambda/\lambda = 2.3\%$ to illustrate the influence of the detector resolution. (b) Data and resolution for $\omega = 3.0°$, the red curve is the simulated reflectivity convoluted with the expected resolution according to Eq. (5). (c) Merged corrected data sets for $\omega = 1.0°$ and $\omega = 3.2°$ and resolution. (For interpretation of the references to color in this figure caption, the reader is referred to the web version of this paper.)

higher angles). In addition the maximum reachable footprint increases from 2 mm to 15 mm. Thus the counting time will be reduced by a factor 35 for samples of at least 15 mm width, relative to the present demonstrator set-up. At the same time the radiation background in the experimental hall is expected to get lower because of the much reduced flux in the guide.

The European Spallation Source will host the neutron reflectometer *Estia* being developed and constructed by PSI [20]. *Estia* will be equipped with a *Selene* type neutron guide.

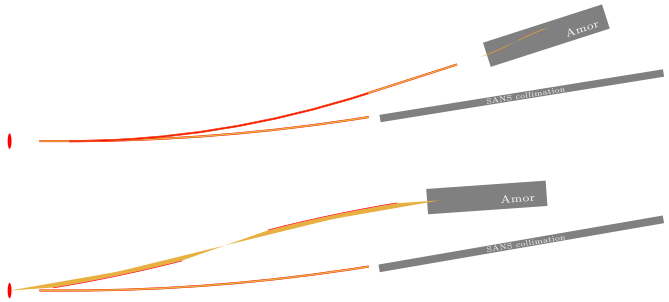

Fig. 12. Sketches to illustrate the actual (top) and planned guide lay-out (bottom) for Amor and the large Small Angle Neutron Scattering instrument at PSI. The gray bars correspond to the granite block for Amor (see Fig. 3) and to the collimation section for SANS, respectively.

7. Conclusion

We recapitulated the concept of using a focused beam and a position-sensitive detector for high-intensity specular reflectometry on a TOF reflectometer. The implementation of both, hardware and a data reduction algorithm on Amor at PSI were presented. The hardware is the combination of the 4 m long demonstrator of the *Selene* guide and a matched polariser with a equiangular spiral shape. Data reduction deviates from conventional measurements essentially in the use of a reference measurement and in the projection of wavelength and angle dependent data array onto a q_z grid. The performance was shown on the example of studies of Li diffusion through Si with a time resolution down to 90 s. The same experiment was used to illustrate the agreement between the calculated and the measured resolution function, respectively.

Acknowledgements

Particularly we thank E. Hüger, F. Strauß and H. Schmidt for providing the material for the experimental examples.

We thank U. Hansen, T. Panzner and P. Korelis for their help during the early tests and measurements with the *Selene* guide.

The *Selene* guide demonstrator was co-financed by the Swiss State Secretariat for Education, Research and Innovation SE RI, as an in-kind contribution to the development of *Estia* to the European Spallation Source ESS in Lund.

This work is based on experiments performed on Amor at the Swiss spallation neutron source SINQ, Paul Scherrer Institute, Villigen, Switzerland.

References

[1] J. Daillant, A. Gibaud, X-Ray and Neutron Reflectivity: Principles and Applications, Lecture Notes in Physics, Monographs 58, Springer-Verlag Berlin Heidelberg, New York, 1999.
[2] R. Cubitt, J. Stahn, Eur. Phys. J. Plus 126 (2011) 111.
[3] Frédéric Ott, Alain Menelle, Nucl. Instrum. Methods Phys. Res. A 586 (1) (2008) 23, Proceedings of the European Workshop on Neutron Optics—NOP '07.
[4] J. Stahn, T. Panzner, U. Filges, C. Marcelot, P. Böni, Nucl. Instrum. Methods Phys. Res. A 634 (1) (2011) Supplement, 1, Proceedings of the International Workshop on Neutron Optics NOP 2010, S12–S16, http://dx.doi.org/10.1016/j.nima.2010.06.221.
[5] J. Stahn, U. Filges, T. Panzner, Eur. Phys. J. Appl. Phys. 58 (2012) 4.
[6] F. Ott, A. Menelle, Eur. Phys. J.—Spec. Top. 167 (2009) 93.
[7] H. Maier-Leibnitz, T. Springer, J. Nucl. Energy Parts A/B 17 (1963) 217.
[8] L.D. Cussen, D. Nekrassov, C. Zendler, K. Lieutenant, Nucl. Instrum. Methods Phys. Res. Sect. A—Accel. Spectrom. Detect. Assoc. Equip. 705 (March) (2013) 121.

[9] C. Zendler, D. Nekrassov, K. Lieutenant, Nucl. Instrum. Methods Phys. Res. Sect. A—Accel. Spectrom. Detect. Assoc. Equip. 746 (May) (2014) 39.
[10] Leo D. Cussen, Thomas Krist, Klaus Lieutenant, Nucl. Instrum. Methods Phys. Res. Sect. A—Accel. Spectrom. Detect. Assoc. Equip. 777 (March) (2015) 6.
[11] M. Gupta, T. Gutberlet, J. Stahn, P. Keller, D. Clemens, Pramana—J. Phys. 63 (2004) 57.
[12] A.A. van Well, Phys. B: Condens. Matter 180–181 (2) (1992) 959.
[13] Mark Koennecke, Frederick A. Akeroyd, Herbert J. Bernstein, Aaron S. Brewster, Stuart I. Campbell, Bjoern Clausen, Stephen Cottrell, Jens Uwe Hoffmann, Pete R. Jemian, David Maennicke, Raymond Osborn, Peter F. Peterson, Tobias Richter, Jiro Suzuki, Benjamin Watts, Eugen Wintersberger, Joachim Wuttke, J. Appl. Crystallogr. 48 (February (1)) (2015) 301.
[14] Giacomo Resta, Boris Khaykovich, David Moncton, J. Appl. Crystallogr. 48 (April (2)) (2015) 558.
[15] J.E. Bateman, R. Dalgliesh, D.M. Duxbury, W.I. Helsby, S.A. Holt, C.J. Kinane, A. S. Marsh, N.J. Rhodes, E.M. Schooneveld, E.J. Spill, R. Stephenson, Nucl. Instrum. Methods Phys. Res. A 698 (January) (2013) 168.
[16] Robert Cubitt, Thomas Saerbeck, Richard A. Campbell, Robert Barker, Philipp Gutfreund, J. Appl. Crystallogr. 48 (December (6)) (2015) 2006.
[17] Erwin Hueger, Lars Doerrer, Johanna Rahn, Tobias Panzner, Jochen Stahn, Gerhard Lilienkamp, Harald Schmidt, Nano Lett. 13 (March (3)) (2013) 1237.
[18] E. Hueger, J. Stahn, H. Schmidt, J. Electrochem. Soc. 162 (2015) A7104.
[19] E. Hueger, L. Doerrer, J. Stahn, T. Geue, H. Schmidt, Defect Diffus. Forum 363 (2015) 49.
[20] Home-page of the instrumentation project Estia for the European Spallation Source, ESS: URL: ⟨https://psi.ch/lns/estia⟩.